The influence of scan length on fabricating thin-walled components in selective laser melting

Zhonghua Li, Renjun Xu, Zhengwen Zhang, Ibrahim Kucukkoc

PII: S0890-6955(17)30175-X
DOI: 10.1016/j.ijmachtools.2017.11.012
Reference: MTM 3312

To appear in: *International Journal of Machine Tools and Manufacture*

Received Date: 23 September 2017
Revised Date: 18 November 2017
Accepted Date: 21 November 2017

Please cite this article as: Z. Li, R. Xu, Z. Zhang, I. Kucukkoc, The influence of scan length on fabricating thin-walled components in selective laser melting, *International Journal of Machine Tools and Manufacture* (2017), doi: 10.1016/j.ijmachtools.2017.11.012.

The influence of scan length on fabricating thin-walled components in selective laser melting

Zhonghua Li [a c *], **Renjun Xu** [b], **Zhengwen Zhang** [b c], **Ibrahim Kucukkoc** [d]

[a] School of Mechanical Engineering, North University of China, 030051, Taiyuan, Shanxi Province, China

[b] Suzhou XDM 3D Printing Technology Co., Ltd, 215143, Suzhou, Jiangsu Province, China

[c] State Key Laboratory on Mechanical Transmission, Chongqing University, 400044, Chongqing, China

[d] Department of Industrial Engineering, Balikesir University, Cagis Campus, Balikesir, Turkey

Abstract

As one of the advanced additive manufacturing (AM) processes, the selective laser melting (SLM) process provides the possibility of manufacturing almost any complex parts in a wide range of metal materials. In the SLM process, undesired distortion and shrinkage are much more likely to occur in forming Ti6Al4V thin-walled parts due to high-temperature gradients and thermal stresses. In this study, a three-dimensional (3D) finite element model based on indirect coupled thermal-structural analysis is applied to study the variations of temperature, stress and strain fields with different scan lengths. At the same time, the corresponding validation experiments were conducted. It was found that the scan length chiefly affects the second peak temperature rather than the highest temperature. The strain is majorly decided by stress generated during the SLM process. The deviations of thin-walled parts are approximately proportional to the scan lengths. The most suitable scan length is between 4mm and 6mm for thin-walled components with specified process parameters, in which case the shrinkage per unit is close to zero.

Keywords: Selective laser melting; finite element analysis; scan length; thin-walled part; additive manufacturing

* *Corresponding author.*

Email: *lizhonghua_6868@163.com, Tel: +8618734199012.*

Contact details for co-authors

Renjun Xu, Email: xurenjun1991@163.com

Zhengwen Zhang, Email: *zhangzw@cqu.edu.cn*

Ibrahim Kucukkoc, Email: *ikucukkoc@balikesir.edu.tr*

The influence **of scan length on fabricating thin-walled components in selective laser melting**

Abstract

As one of the advanced additive manufacturing (AM) processes, the selective laser melting (SLM) process provides the possibility of manufacturing almost any complex parts in a wide range of metal materials. In the SLM process, undesired distortion and shrinkage are much more likely to occur in forming Ti6Al4V thin-walled parts due to high-temperature gradients and thermal stresses. In this study, a three-dimensional (3D) finite element model based on indirect coupled thermal-structural analysis is applied to study the variations of temperature, stress and strain fields with different scan lengths. At the same time, the corresponding validation experiments were conducted. It was found that the scan length chiefly affects the second peak temperature rather than the highest temperature. The strain is majorly decided by stress generated during the SLM process. The deviations of thin-walled parts are approximately proportional to the scan lengths. The most suitable scan length is between 4mm and 6mm for thin-walled components with specified process parameters, in which case the shrinkage per unit is close to zero.

Keywords: Selective laser melting; finite element analysis; scan length; thin-walled part; additive manufacturing

1. Introduction

AM technologies have been successfully utilized in product development and fabricating process nowadays. SLM is the most sophisticated AM technology that allows making complicated parts directly from the metal powder material without using any intermediate binders, this is needed for manufacturing the metal component using the selective laser sintering (SLS) process [1,2]. Due to its special process characteristics, SLM has the capability to produce metal components of any intricate shape, such as components with complex porous structures that would be impossible to fabricate in conventional manufacturing processes [3]. In addition, SLM can also be used in making thin-walled structures. Nevertheless, the great temperature gradients and high stresses could cause undesired distortion and shrinkage for the thin-walled structure; these are the major shortcomings of SLM technology. The process parameters of SLM (such as laser power, scan length, scan speed, hatch spacing, laser spot size, layer thickness and scan strategy) all influence the evolution of temperature gradients and residual stresses [4].

Thin-walled parts have been widely used in aerospace. However, in the traditional processes, it is difficult to manufacture high precision thin-walled products due to the effect of low rigidity and the cutting force. SLM technology has been successfully applied in fabricating thin-walled metal components. Liu et al. [5] have studied the effects of powder concentation distribution on the fabrication of thin-walled parts in coaxial laser cladding. Chao et al. [6] have investigated the influences of process parameters on the formed wall thickness and deposition accuracy of droplets, a micro thin-walled structures with a wall thickness of 400μm was manufactured by micro-droplet deposition. Luo et al. [7] apply laser-induced forward transfer (LIFT) for manufacturing complex-shaped high-aspect-ratio pillars, and demonstrate its potential for functional microdevices that consist of multiple metals. Clijsters et al. [8] have studied strategies to build thin walls with the correct dimensions using locally optimised scan parameters; walls down to a size of 90μm can be manufactured by adapting the laser power and scan speed. Abele et al. [9] and Yadroitsev et al. [10] have studied the proper process parameters for thin-walled parts through experiments. Nevertheless, this is time consuming, expensive, and it is hard to acquire global variations. To overcome the shortcomings of conducting an experiment, the finite element method (FEM) is most commonly recommended in order to optimise the process parameters. The distribution and history of the temperature field obtained from a 3D heat transfer FEM model with the evolution of thermal conductivity fit well with the measured temperature field [11]. Song et al. [12] have studied the temperature distribution of a single track of laser scanning on Ti6Al4V powder by including temperature dependent heat capacity in ANSYS commercial software. It was found that the qualities of built parts mainly depend on the temperature distribution during the fabricating process. Contuzzi et al. [13] have developed a subroutine in the FEM model to simulate the powder-liquid-solid change. A more comprehensive understanding of the thermal field has been achieved by creating a 3D model and considering the interval time for recoating powder [14]. Hussein et al. [4] have optimised the SLM process parameters to meet the special functional requirement by developing a 3D non-linear transient FEM model, which was developed by ANSYS parametric design language (APDL). As seen from this survey, although FEM has been widely adopted in the SLM process, there is a very limited number of research studies that use this method to study the relationship between the scan lengths and the distributions of temperature and stress fields of thin-walled parts in the SLM process.

In this study, a 3D non-linear FEM model based on sequentially coupled thermal-structural field analysis is developed to predict the temperature distributions, thermal stresses, molten pool dimensions and strains of a single layer of thin-walled parts built on a Ti6Al4V powder bed. In this simulation, the latent heat of fusion and the change of material physical properties are taken into account. The corresponding experiments have been conducted to verify the correctness of the simulation. Meanwhile, the suitable thermophysical parameters of Ti6Al4V are generalized. A finite element simulation and analysis of global changes in temperature, stress and strain caused by the different scan lengths of thin-walled parts built in the SLM process are the key points of this study. An appropriate scan length is obtained from the experiment's results and the simulation data.

2. The 3D FEM model for the SLM process

ANSYS provides the indirect sequentially coupled thermal-structural analysis method that is suitable for analysing both the thermal and the stress fields in the SLM process. Firstly, a non-linear transient thermal analysis is conducted to acquire the global temperature variation generated during laser irradiating. Afterwards, a stress and a strain analysis are developed with an automatic change element type from thermal to structural, and the temperatures obtained from the previous transient thermal analysis are applied to the structural analysis model as a thermal load. The 3D finite element model representing the processing powder layer of a thin-walled component formed in SLM process can be seen in Fig. 1. In order to obtain the best calculating precision in the shortest computing time, the elements irradiated by the laser beam are finely meshed with hexahedral element sizes equal to 25μm, and a coarser mesh is applied to the surrounding powder. The parameters used in the finite element analysis are summarised in Table 1.

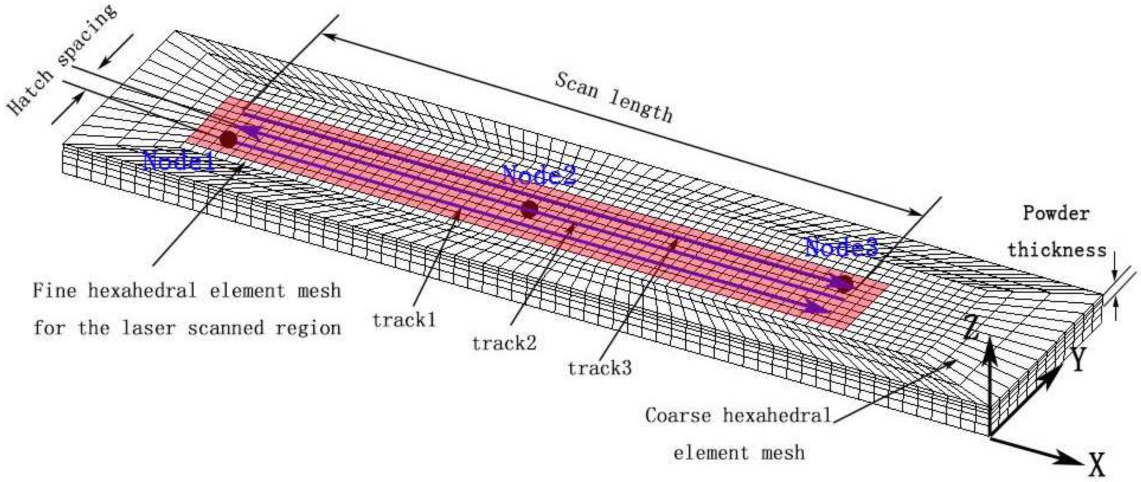

Fig. 1. The 3D FEM model

Table 1. Parameters of FEM

Parameter	Value
Laser power, p	170 W
Preheating temperature	35 ℃
Scan speed, v	1250 mm/s
Scan length, l	2, 4, 6, 8, 10, 20, 30, 40, 50, 60, 70, 80, 90, 100 mm
Number of tracks, n	3 tracks
Power bed thickness, t	30 μm
Hatch spacing, h_s	0.1 mm
Laser spot diameter, d	0.1 mm
Thermal element type, 3D	Solid 70
Structural element type, 3D	Solid 45
Surface effect element	Surf 152

2.1. Physical description of heat transfer in SLM

Fig. 2 depicts the schematic diagram of heat transfer in the SLM process. As the metal powder bed surface is irradiated by the laser beam, a considerable part of the laser's energy is reflected and only a tiny percentage of energy is absorbed. Metal powders are melted by the absorbed energy, resulting in a micro-sized molten pool. The raw materials experience phase changes from powder to liquid and finally to solid. Metallurgical bonding is formed between the neighboring scan tracks and the adjacent powder layers during the solidification process [15]. A 3D finite element thermal analysis model is developed on the basis of this schematic of thermal behavior in the powder bed.

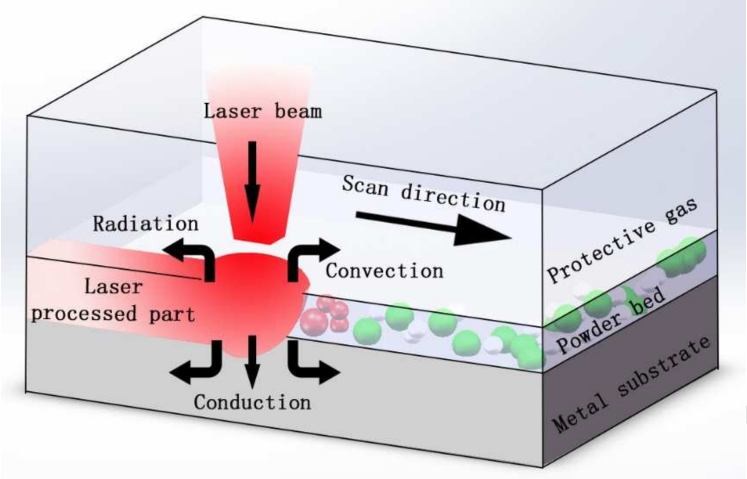

Fig. 2. Schematic representation of heat transfer in the powder bed

2.2. Thermal modelling

The governing equation satisfies the classical Fourier heat equation applied as follows [12,4]:

$$\rho c \frac{\delta T}{\delta t} = \frac{\delta}{\delta x}\left(k_x \frac{\delta T}{\delta x}\right) + \frac{\delta}{\delta y}\left(k_y \frac{\delta T}{\delta y}\right) + \frac{\delta}{\delta z}\left(k_z \frac{\delta T}{\delta z}\right) + \bar{Q}\,, \tag{1}$$

where ρ is the material density; c is the special heat capacity; T is the temperature; t is the interaction time; k_x, k_y and k_z are the thermal conductivities of x, y and z directions, respectively; and $\bar{Q}$ is the heat source density. In this simulation, the Ti6Al4V powder bed is assumed to be a homogeneous and isotropic medium. Thus, the thermal conductivities of the three directions are supposed to be the same. Eq. (1) can be simplified as in Eq. (2):

$$\rho c \frac{\delta T}{\delta t} = k \frac{\delta^2 T}{\delta x^2} + k \frac{\delta^2 T}{\delta y^2} + k \frac{\delta^2 T}{\delta z^2} + \bar{Q}\,, \tag{2}$$

where k is the thermal conductivity.

2.3. Laser energy modelling

The Gaussian distribution of energy is the most widely used model to represent the laser heat flux in FEM [4, 12, 14, 15]. The heat flux distribution of this model is illustrated in Fig. 3(a), drawn by the following equation:

$$q = \frac{2Ap}{\pi {r_0}^2} exp\left(-\frac{2r^2}{{r_0}^2}\right), \tag{3}$$

where A is the laser absorptivity of the powder material, r_0 is the beam spot radius and r is the radial distance.

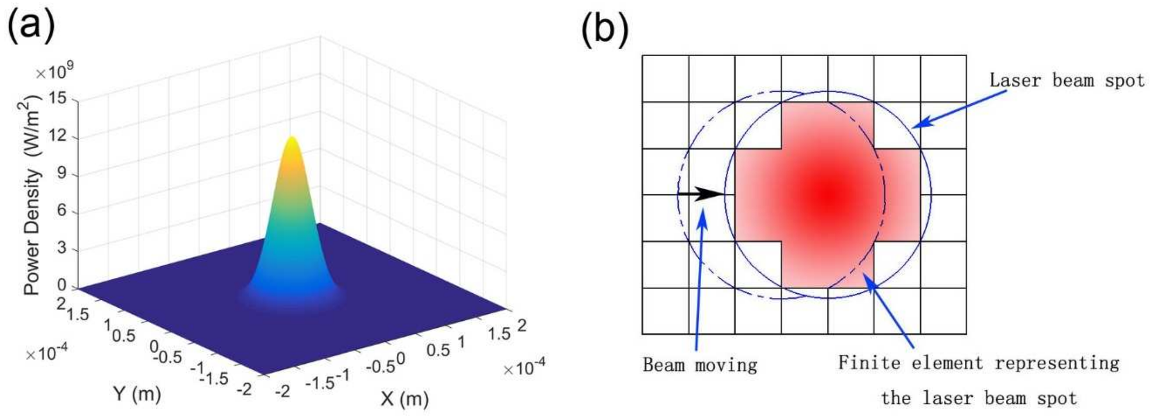

Fig. 3. (a) Gaussian laser energy distribution profile; (b) Movement of laser beam represented by twelve elements

The laser energy absorptivity is known to depend on multiple factors, such as laser wavelength, oxidation level, material type, and so on [14, 17-19]. The absorptivity of the Ti6Al4V powder has not been determined as it changes a great deal when the metal melts [14, 20]. Therefore, the absorptivity of pure titanium powder at a laser wavelength of 1.06μm, as proposed by Fischer et al. [21], is considered to be the representative absorptivity value for the Ti6Al4V powder material. In this research, the laser beam is expected to irradiate twelve elements as shown in Fig.3 (b).

2.3.1. Temperature-dependent material properties of the Ti6Al4V alloy

The thermophysical properties of the material can be divided into field and non-field characteristics [14, 22]. The thermal conductivity, which is the most crucial parameter for heat dissipation in SLM, is a field property. Nonetheless, the special heat capacity and enthalpy are non-field properties, and are controlled by the given composition of the material. Many models have been proposed to explain the relationship of thermal conductivities between the powder bed and the solid [4, 15]. The field properties are very hard to express accurately due to the complex pore geometries of powder materials. Thummler and Oberacker [22] represent the thermal conductivity of the powder by a simplified generic relationship as follows:

$$k_{powder} = k_{solid}(1-\varphi)\,, \tag{4}$$

where k_{powder} and k_{solid} are the thermal conductivities of the powder and the solid materials, respectively; φ is the porosity of the powder and can be computed as follows:

$$\varphi = \frac{\rho_{solid} - \rho_{powder}}{\rho_{solid}}\,, \tag{5}$$

where ρ_{solid} and ρ_{powder} are the densities of the solid and the powder materials. The density is supposed to be proportional to the temperature when the temperature is below the melting point.

The effective thermal conductivity of a loose powder bed is basically independent of the material but is controlled by the void fraction and gas in the pores [14, 23]. It was found that for powders of 10-50μm diameter, the effective thermal conductivity ranges typically from

0.1 to 0.2 W/(m·K) at room temperature and 0.3 W/(m·K) is expected as the effective thermal conductivity at melting point for the Ti6Al4V powder [24]. Therefore, the thermal conductivity of the Ti6Al4V powder material begins from a low value for the powder's status but increases rapidly at the melting point. In this FEM, once the elements are irradiated by the laser beam, the element type is changed from powder to bulk automatically through the subroutine written by APDL. Fig. 4 shows variations of the thermophysical properties with temperature for the Ti6Al4V powder and the solid [14, 25].

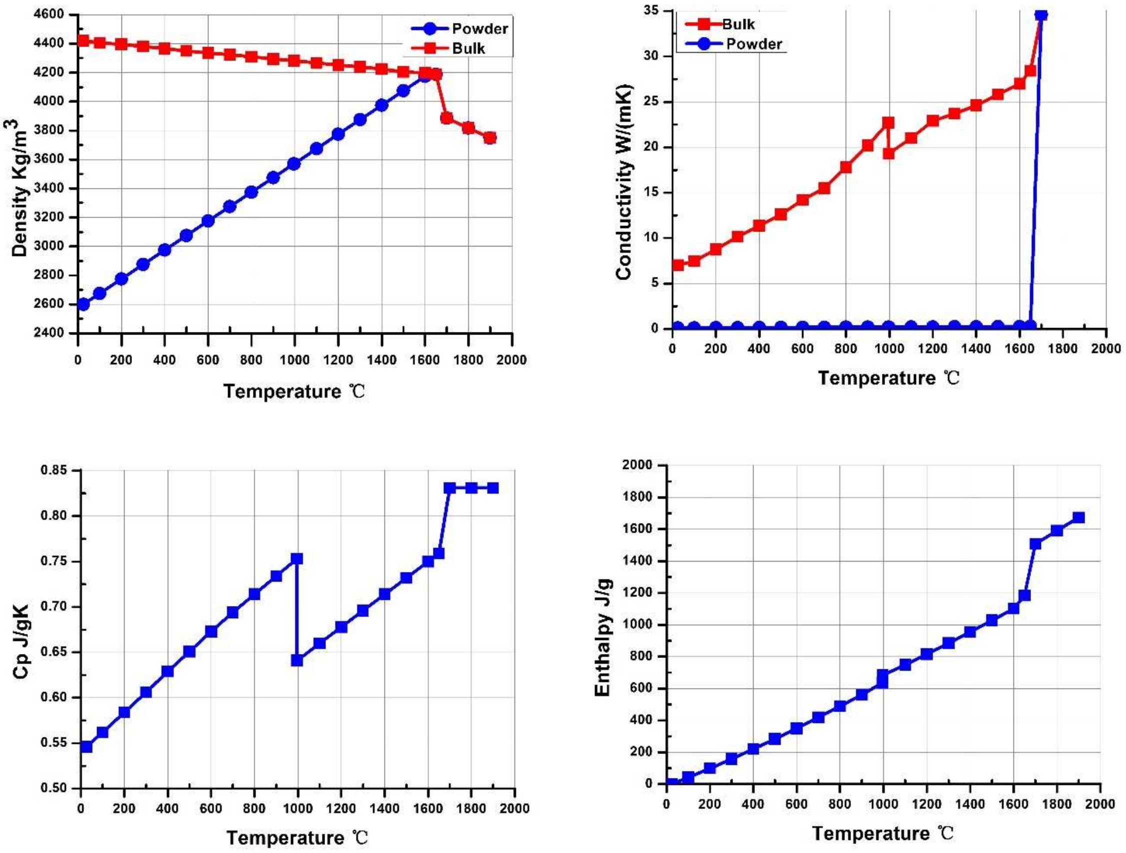

Fig. 4. Thermophysical properties for Ti6Al4V at different temperatures

Regarding the latent heat caused by the phase change in SLM, ANSYS will calculate the latent heat by defining the enthalpy at different temperatures. The relationship between the enthalpy (H), the density (ρ), and the special heat (c) is expressed as follows:

$$\mathrm{H} = \int \rho c(T)\, dT\ . \tag{6}$$

2.3.2. Initial and boundary conditions

The initial temperature of finite element models is equal to the preheating temperature, which is 35℃.

The heat transfer at the top surface of the powder bed can be applied as:

$$-\mathrm{k}\frac{\partial T}{\partial z}\bigg|_{z=z_s} = h(T_s - T_0)\ , \tag{7}$$

where h is the convective heat transfer coefficient at the top surface of the powder bed and is taken as 8 W/(m·K); T_s is the temperature of the powder bed; and T_0 is the ambient temperature of the process chamber.

The substrate is much larger than the manufacturing zone. Meanwhile, the conductivity of the Ti6Al4V material is quite low. Hence the heat transfer at the sides and bottom of the model can be assumed to be negligible.

Heat flux and convection loads exist on the powder bed surface simultaneously. ANSYS provides a surface effect element to solve a situation where the same element may be affected by various loads and surface effects at the same time. The surface effect element employed in this simulation is summarised in Table 1.

2.4. Structural analysis

2.4.1. Element birth and death

The method of element birth and death is applied to simulate the unprocessed loose powder material that has no influence on the thermal deformation during the structural analysis. The laser beam moves on the powder bed with the activation of corresponding elements at the desired time points. Un-activated elements do not add to the overall stiffness matrix of the model. This simulation technology has been applied by Roberts et al. [14] in the multi-layers temperature field simulation of the Ti6Al4V powder material in additive manufacturing.

2.4.2. The fundamentals of thermal stress analysis

The temperatures from the thermal analysis become the loads for the structural analysis. The same finite element mesh used in the thermal analysis is employed in the structural analysis, except for the element type (as listed in Table 1) and the boundary conditions. The relationship between the stress and the strain is defined as [26]:

$$\{\sigma\} = [D]\{\varepsilon^e\}\,, \tag{8}$$

where $\{\sigma\}$ is the stress vector; $[D]$ is the elasticity matrix; and $\{\varepsilon^e\}$ is the elastic strain vector and for the ideal elastic-plastic body,

$$\{\varepsilon^e\} = \{\varepsilon\} - \{\varepsilon^{\mathrm{p}}\} - \{\varepsilon^t\}\,, \tag{9}$$

where $\{\varepsilon\}$, $\{\varepsilon^{\mathrm{p}}\}$ and $\{\varepsilon^t\}$ are the total strain vector, the plastic strain vector, and the thermal strain vector, respectively.

Eq. (9) can also be written as:

$$\{\varepsilon\} = [D]^{-1}\{\sigma\} + \{\varepsilon^p\} + \{\varepsilon^t\}\,, \tag{10}$$

since the material is assumed to be isotropic, the above stress-strain equation can be expressed in Cartesian coordinates as [26-30]:

$$\begin{aligned}
\varepsilon_x &= \frac{1}{E}\left[\sigma_x - \mu\left(\sigma_y + \sigma_z\right)\right] + \varepsilon_x^p + \varepsilon^t \\
\varepsilon_y &= \frac{1}{E}\left[\sigma_y - \mu(\sigma_x + \sigma_z)\right] + \varepsilon_y^p + \varepsilon^t \\
\varepsilon_z &= \frac{1}{E}\left[\sigma_z - \mu\left(\sigma_x + \sigma_y\right)\right] + \varepsilon_z^p + \varepsilon^t \\
\gamma_{xy} = \frac{\tau_{xy}}{2G} + \gamma_{xy}^p,\ \gamma_{xz} &= \frac{\tau_{xz}}{2G} + \gamma_{xz}^p,\ \ \gamma_{yz} = \frac{\tau_{yz}}{2G} + \gamma_{yz}^p,
\end{aligned} \tag{11}$$

where E, G, μ are the elastic modulus, shear modulus and Poisson's ratio, respectively. A typical calculation method of thermal strain from Eq. (11) is,

$$\varepsilon^t = \alpha_e \Delta T = \alpha_e(T - T_{ref}) \tag{12}$$

where α_e is the coefficient of thermal expansion; T is the temperature at time t, and T_{ref} is the reference temperature at t=0.

When the stress exceeds yield limit of the material, plastic deformation will occur. According to Prandtl-Reuss equations in plasticity theory, the plastic strain increment is proportional to the instant deviator stress and shear stress as follows [29]:

$$\begin{gathered}
\frac{d\varepsilon_x^p}{\sigma_x'} = \frac{d\varepsilon_y^p}{\sigma_y'} = \frac{d\varepsilon_z^p}{\sigma_z'} = \frac{d\gamma_{xy}^p}{\tau_{xy}} = \frac{d\gamma_{yz}^p}{\tau_{yz}} = \frac{d\gamma_{zx}^p}{\tau_{zx}} = d\lambda \\
\sigma_x' = \sigma_x - \sigma_m \\
\sigma_y' = \sigma_y - \sigma_m \\
\sigma_z' = \sigma_z - \sigma_m
\end{gathered} \tag{13}$$

where σ_x', σ_y' and σ_z' are the deviator stresses of x, y and z directions in Cartesian coordinates, respectively; $d\lambda$ is the instant positive constant of proportionality; σ_m is the mean value of stress and is defined as:

$$\sigma_m = \frac{\sigma_x + \sigma_y + \sigma_z}{3} \tag{14}$$

Then Eq. (11) may be substituted by,

$$\begin{aligned}
\varepsilon_x &= \frac{1}{E}\left[\sigma_x - \mu\left(\sigma_y + \sigma_z\right)\right] + \int \sigma_x' d\lambda + \alpha_e \Delta T \\
\varepsilon_y &= \frac{1}{E}\left[\sigma_y - \mu(\sigma_x + \sigma_z)\right] + \int \sigma_y' d\lambda + \alpha_e \Delta T \\
\varepsilon_z &= \frac{1}{E}\left[\sigma_z - \mu\left(\sigma_x + \sigma_y\right)\right] + \int \sigma_z' d\lambda + \alpha_e \Delta T \\
\gamma_{xy} = \frac{\tau_{xy}}{2G} + \int \tau_{xy} d\lambda,\ \ \gamma_{xz} &= \frac{\tau_{xz}}{2G} + \int \tau_{xz} d\lambda,\ \ \gamma_{yz} = \frac{\tau_{yz}}{2G} + \int \tau_{yz} d\lambda
\end{aligned} \tag{15}$$

In the structural analysis, there will be a residual deformation after cooling when the yield point is met. Both the elastic and the plastic deformations affect the deformation zone. The

ANSYS program analyzes the deformation of the material after cooling according to the elastic-plastic strain state.

The mechanical properties depending on the temperature are required for the stress analysis as listed in Table 2.

Table 2. Temperature-dependent mechanical properties of Ti6Al4V alloy

Temperature (℃)	**25**	**200**	**500**	**800**	**995**	**1200**	**1400**	**1650**	**1900**
Thermal expansion, α_e ($1℃^{-1} \times 10^{-6}$)	2.9	3.4	4.4	5.7	6.9	7.65	7.9	8.6	9
Elastic modulus, E (GPa)	114.7	105.3	89	75	72.3	64.6	56.8	45.4	0
Poisson's ratio, μ	0.32	0.33	0.34	0.35	0.38	0.39	0.40	0.41	0.5
Yield strength, σ_y (GPa)	11.47	10.53	8.9	7.5	7.23	6.46	5.68	4.54	0
Shear modulus, τ(MPa)	887	847	778	334	38	27	17	3.8	0.38

3. Details of the experiment

3.1 Material properties of the Ti6Al4V alloy

The material used in this study is the Ti6Al4V alloy powder produced using the gas atomisation method. The powder particles show a good spherical morphology as depicted in Fig. 5 with different magnifications. The titanium alloy has many excellent characteristics including low density, high strength/density ratio, etc. The average size of powder particles is approximately 20μm. The process chamber is filled with argon as a protective gas to keep the O_2 level below 0.1% for avoiding oxidization during the whole building process.

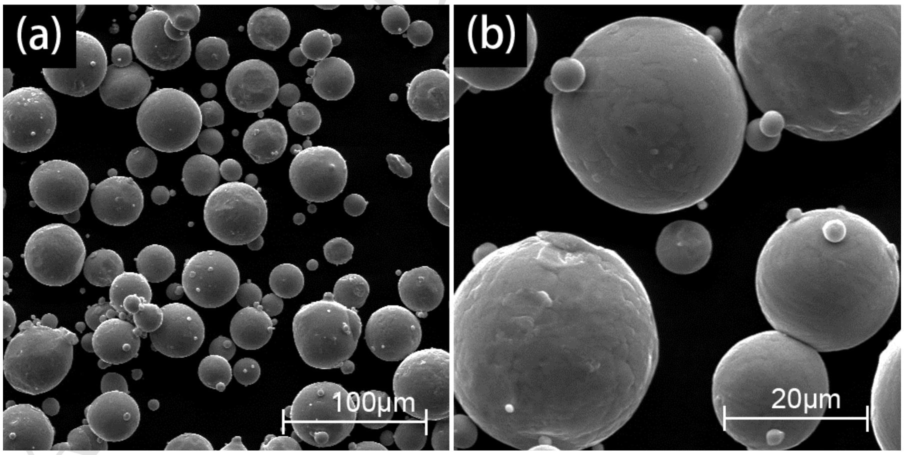

Fig. 5. Morphology of Ti6Al4V powder at low (a) and high (b) magnification of scanning electron microscopy (SEM)

3.2 Experiment

Test specimens have a 0.3×10 mm cross section with different lengths equal to the scan lengths. The lengths of the specimens and the process parameters are listed in Table 1. The specimens are shown in Fig.6. Each dimension is measured three times by a Vernier caliper and the average is considered. The deviation of the thin-walled part in the scan length direction is calculated as:

$$\mathrm{d} = L_d - L_m \tag{16}$$

The percentage shrinkage per unit length can be given by Eq. (17).

$$\mathrm{s} = \frac{L_d - L_m}{L_d} \times 100\% \tag{17}$$

where L_d is the designed length of thin-walled part and L_m is the measured length of the component after cooling.

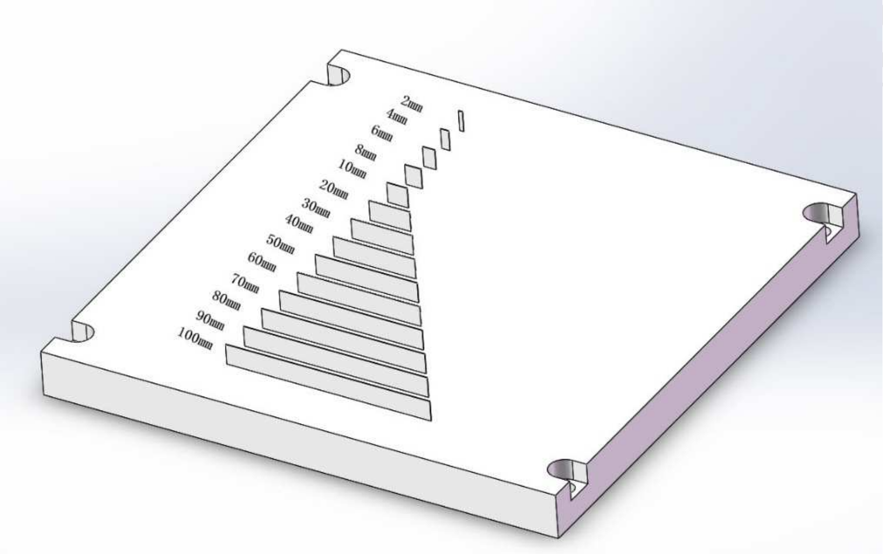

Fig. 6. Shrinkage calibration test specimens

4. Results and discussion

4.1. Temperature distribution

Temperature distributions in the powder bed and the solidified layers change quickly with time and space in the SLM process. The resultant heat affected zone and the maximum temperature location move with the moving laser beam synchronously. Fig. 7 shows the temperature distribution at the beginning of the laser exposure, from which, high-temperature gradients can be clearly seen due to the applied Gaussian heat source. The temperature of the powder particles rises instantly upon being irradiated by the laser beam, causing a molten pool when the temperature exceeds the melting point of Ti6Al4V (1660℃). Since the powder bed is supposed to be a homogeneous and isotropic medium, the surface profile of the molten pool is a circle. The highest temperature at the start of track1 reached 2700℃ and far surpassed the melting temperature of Ti6Al4V. However, the maximum temperature of the powder bed increased to 2726℃ at the end of track 1 as depicted in Fig.8(a), 2732℃ at the end of track 2 as shown in Fig.8(b), and 2737℃ at the end of the last track as shown in Fig.8(c). The increase in the maximum temperature can be attributed to heat accumulation. The powder particle is preheated by the laser beam before it melts, and it will retain heat for a long time because of its relatively low conductivity. According to Fig. 7, the heat affected zone is investigated in the temperature from 35℃ to 1650℃. The preheat temperature of the next laser exposure spot is extremely high, but the temperature increment from the first to the last spot (see Fig. 7 and Fig. 8) is only 37℃. This phenomenon is caused by the increased thermal conductivity of the laser processed regions compared with the untreated Ti6Al4V powder material [4]. Evaporation happens in the building process though the maximum temperature (2737℃) calculated from FEM is lower than the evaporation point. This can be ascribed to the inhomogeneity of the powder bed caused by dust particles and broken metal powder particles, etc. Un-spherical powder particles can absorb more heat from the laser irradiation as the concave surface is conducive to energy accumulation. The temperature of these particles rises rapidly, and can reach or even exceed the evaporation point of Ti6Al4V.

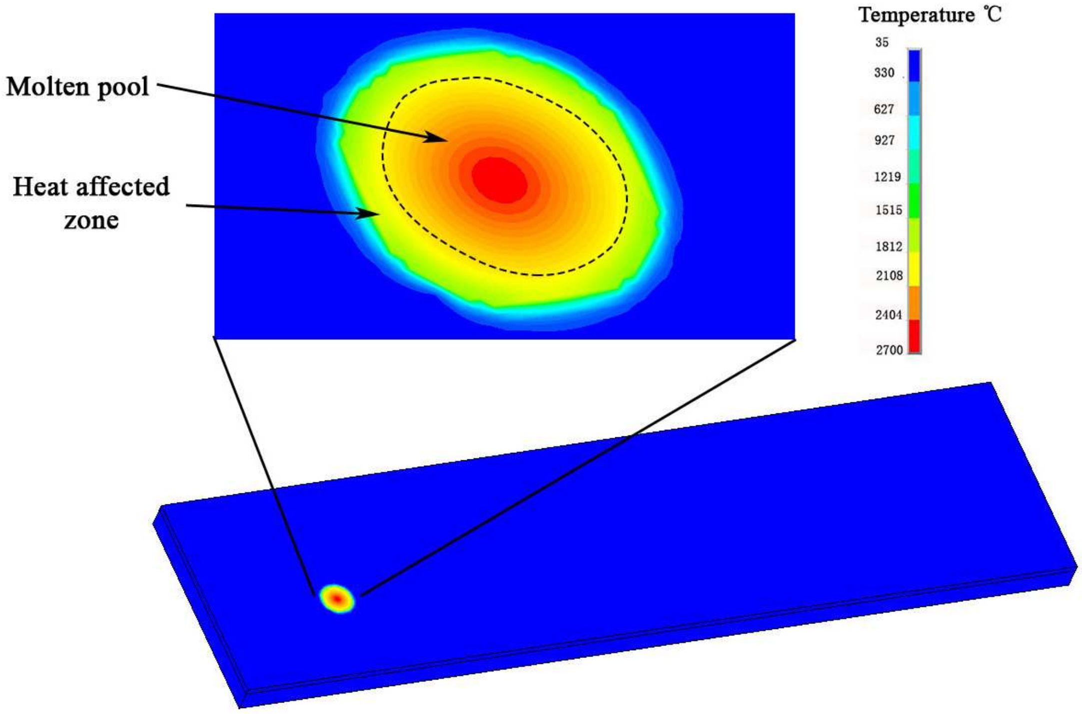

Fig. 7. Temperature distribution at the beginning of the laser scanning

Both the temperature field and the molten pool move with the laser source simultaneously, but the molten pool slightly lags behind the laser beam due to the interaction time between the powder and the laser beam. It is further found that the thermal gradient in the front of moving laser beam is much steeper than that in the reverse directions, as shown in Fig. 8. The trend of temperature distribution can be explained by the fact that the solidified material possesses greater thermal conductivity than the raw powder material [14]. This situation was also presented in the other temperature field simulations [4, 24]. As shown in Fig. 8(c), substrate temperature elevates faster than the powder material on account of the different conductivities between the bulk and the powder material (see Fig. 5). Since a manufacturing layer requires 4.8ms for thin-walled part (length=2mm), the powder phase changes momently, and the rapid solidification technique is beneficial to the mechanical properties of parts owing to the structural modifications [29].

Temperature variations at Node1, Node2, and Node3 (see Fig. 1) during the whole manufacturing process are depicted in Fig. 9. The irradiated spot’s temperature increases rapidly, and a certain region around the spot is in the molten state. The liquid phase may maintain about 0.3ms and then solidify into the entity. The second peak temperature of Node 2 reaches the melting point. However, the second maximum temperatures of Node1 and

Node3 are lower than the melting point, since the cooling periods are long enough to dissipate heat before reheating for Node1 and Node3.

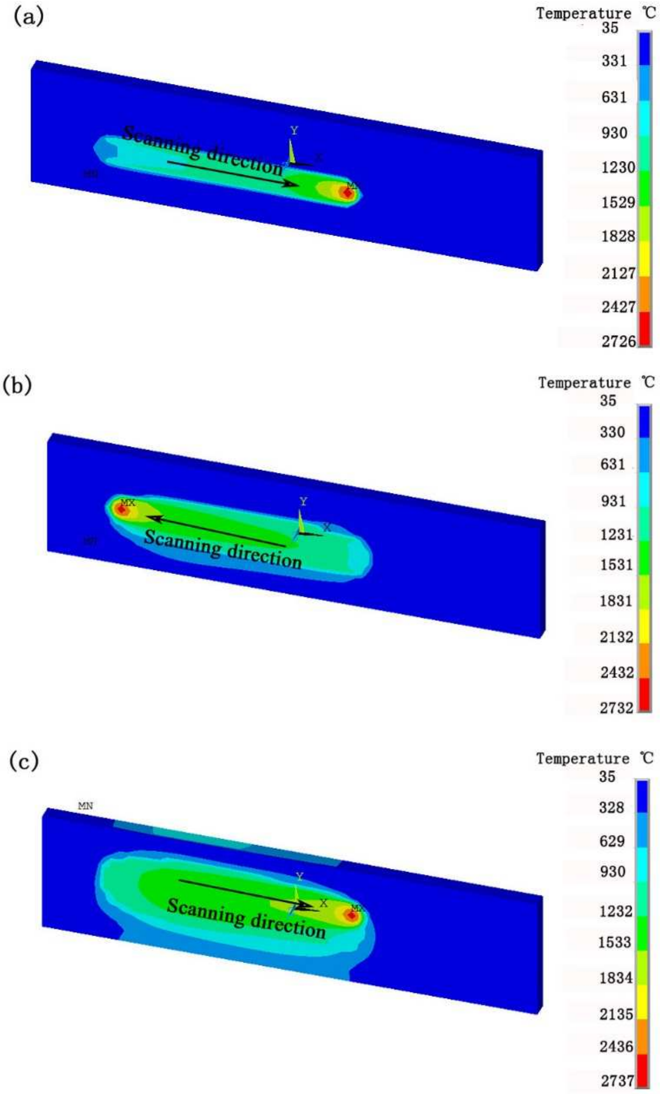

Fig. 8. Temperature distribution in the SLM process at the end of (a) first track, (b) second track and (c) last track

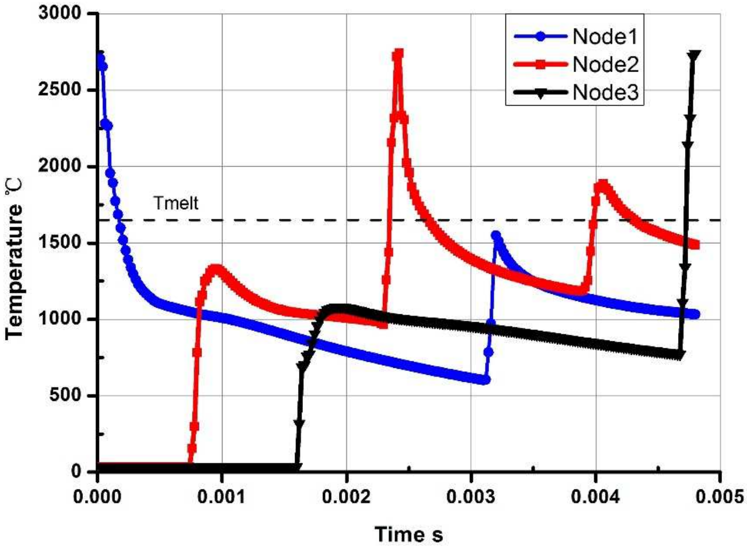

Fig. 9. Variations of temperature in a single layer at Node1, Node2 and Node3

The various heating and cooling cycles of diversified scan lengths taking place in the three nodes during laser scan are displayed in Fig. 10(a), Fig. 10(b) and Fig. 10(c). The maximum temperature is similar for various scan lengths as shown in Fig. 10(d). The difference between the peak temperatures of Node2 and Node3 becomes smaller as the scan length increases. It provides sufficient cooling time when the scan length exceeds a threshold value. The scan length mainly affects the second peak temperatures described in Fig.10(b).

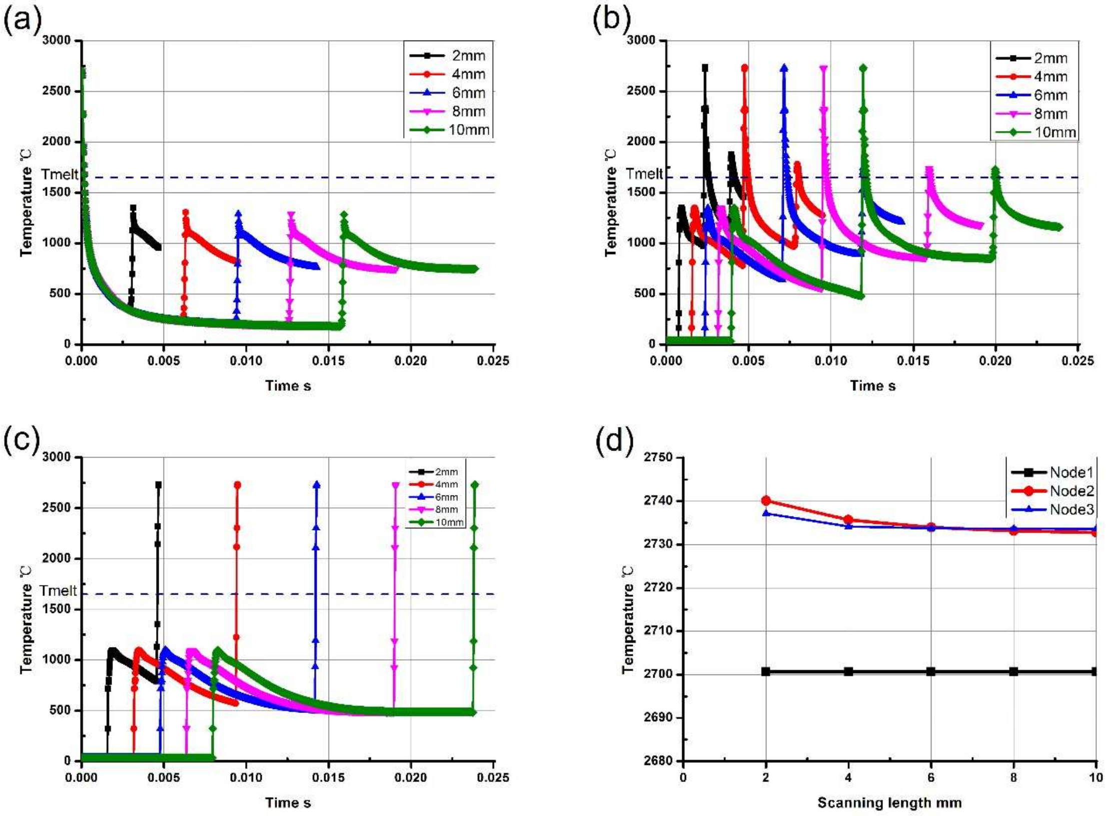

Fig. 10. Temperature variations in a single layer at (a) Node1; (b) Node2; (c) Node3 of different scan lengths; (d) the maximum temperature of multiple scan lengths

The heating and cooling cycles continue in all the tracks during the fabricating process. The irradiated points suffer from rapid temperature cycles. These thermal cycles are in connection with commensurate thermal stress changes [30]. The long scan track has negative effect on the uniformity of the temperature field, while a shorter scan length tends to generate a more homogeneous temperature field [4]. There is some deviation due to the acceleration and deceleration of the scanning mirror during scanning the edges of a layer. The nodule is easy to generate at the edges of the part due to the inertia of the scanning head. In order to reduce the influence of the inertia of the scanning mirror, the scan length should not be too short. Therefore, SLM technology should have a finely tuned scan length.

4.2. Molten pool dimension

Fig. 11 (a) describes the molten pool temperature distribution after scanning track 3 of the single layer. The molten pool dimension is obtained through measuring the size of the melting point isotherm in the temperature distribution cloud plot. The length of the molten pool is parallel to the scanning direction, whilst the width is perpendicular to the laser moving track. The depth of the molten pool is measured from the powder surface to the molten depth inside the powder bed along the layer thickness direction. The length, width and depth of the molten pool obtained from finite element model are 379.7μm, 188.9μm and 64.7μm, respectively. The width of the fabricated track is larger than the hatching space (100μm), thus the solidified section can be re-melted. The surface morphology of the built part is presented in Fig. 11 (b). It is found that the front contour profile of the molten pool resembles an oval shape. The similar molten pool profile is also presented in the finite element model as shown in Fig. 11 (a). The schematic of the scanning strategy with the measured molten pool size from the FEM is illustrated in Fig.1 1 (c). There are no un-molten powders inside the fabricated components with the process parameters listed in Table 1. Therefore, the fully dense parts can be built. In fact, due to the effects of thermal expansion and liquid surface tension, the top contour profile is torus rather than plane [31]. The modified model is depicted in Fig.11 (d). The size of the molten pool is controlled by two main parameters: laser power and scan speed [4, 32].

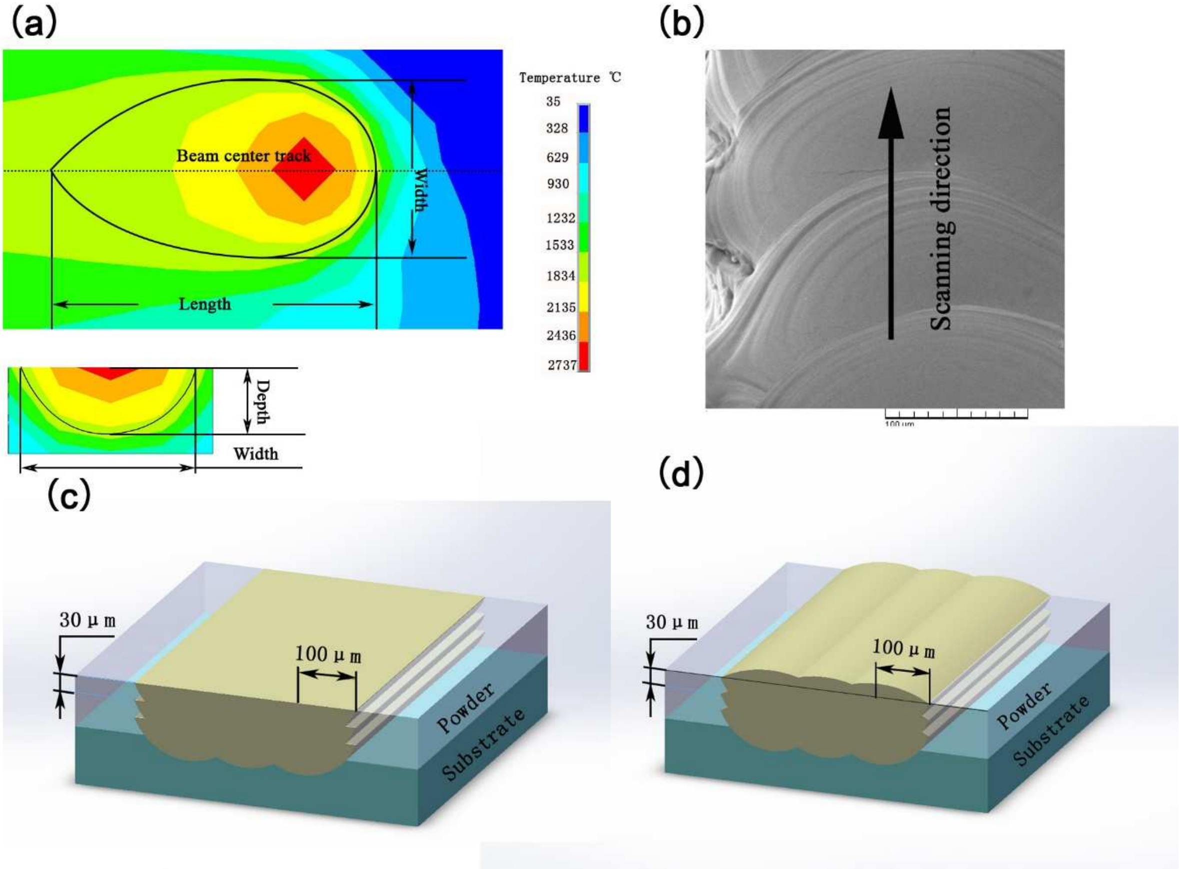

Fig. 11. (a) Molten pool temperature contours at the ending of the last track in FEM (scan length =2mm); (b) Surface morphology of the part; (c) Schematic of the scanning strategy with using the measured molten pool size and (d) The modified schematic

4.3. Stress and strain analysis

Fig.12 illustrates the strong changes in the level of the three directional stresses within a single layer acquired from the finite element model. The X-component, Y-component, and Z-component of stresses at Node2 are cyclic compressive-tensile-compressive stresses. As predicted by Hussein et al. [4], the stress in the molten zone is tensile and it will convert into compressive stress at the boundary of the irradiated zone because of the equilibrium principles of force and momentum as described in Fig. 13. The top layer will be plastically deformed once the material yield stress is reached. The material yield stress is lowered because of the high temperature. During the cooling and shrinking period, a bending angle towards l the aser beam develops due to the fact that the upper layer is cooling contraction, yet the bottom layer is being heated by the energy obtained from the irradiated surface. Since the non-scanning zone is loose material, Node2 maintains a zero-stress state at the beginning of the process and the element birth and death technology of FEM is adopted to simulate this situation.

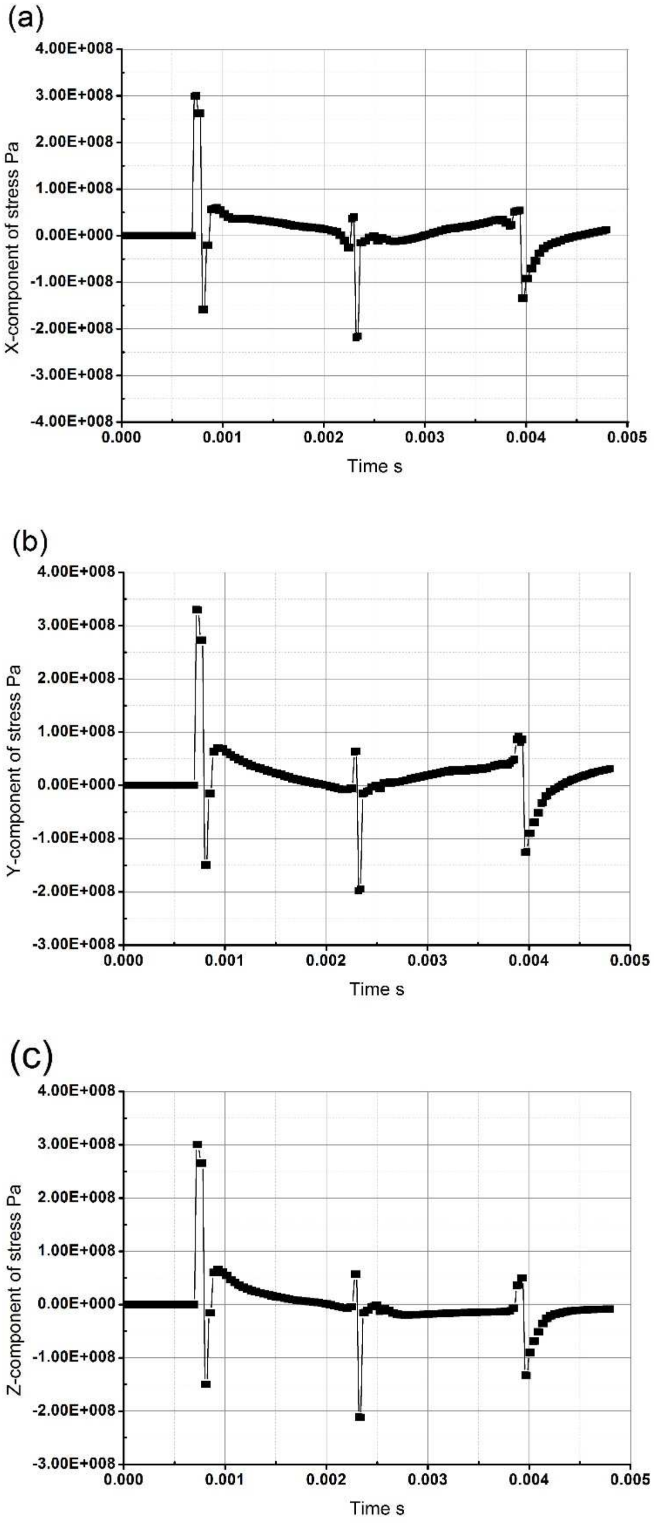

Fig. 12. Stress distribution at Node2 (scan length =2mm) (a) X-component of stress; (b) Y-component of stress and (c) Z-component of stress

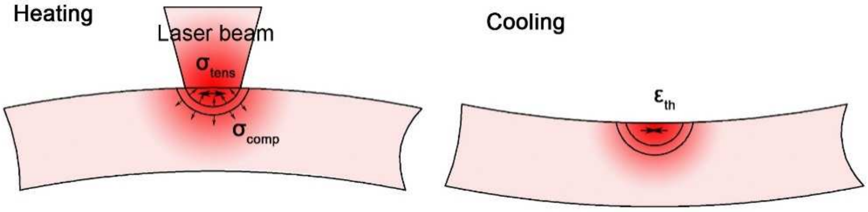

Fig. 13. Schematic of stress distribution

Node2 is firstly heated when the heating source moves on the centre node of track 1. The X-component of stress changes from compressive into tensile when Node2 is heated as indicated in Fig. 12(a). As the laser beam moves away, the part cools down and the node remains compressive. The X-component of stress gradually releases after scanning the last track. As the material is expected to be isotropic, similar trends are also observed in the Y and Z directional stresses of Node2 as shown in Fig. 12(b) and Fig. 12(c). The three directional compressive stresses reach maximum values when Node2 is firstly heated and reach 300MPa, 330MPa and 300MPa respectively, whereas the peak tensile stresses of the three directions are all found at scanning Node2 and reach 219MPa, 200MPa and 212MPa, respectively.

Fig.14 depicts stresses variations and the history of Node2 in the X, Y, Z-components of different scan lengths. The maximum compressive stresses are basically the same. However, the peak tensile stresses increase with the scan lengths (ranging from 2-10mm). This can be explained by the fact that a long scan length might lead to a large temperature gradient, which is the major influencing factor of the stress field. As the scan length is long enough to fully dissipate the heat, the maximum tensile stresses should remain constant. Nevertheless, they begin to slightly decrease as described in Fig. 14(d). This can be attributed to stress relaxation. The residual stress of Node2 in Z direction decreases with scan length, but that in the X and Y directions increase as presented in Fig. 14(e). The peak tensile and residual stresses all tend to stabilise while continuing to increase the scan length. For this reason, a short scan length is more suitable for the SLM process than a long length. To avoid a long scan length, a partition scan strategy can be adopted [33].

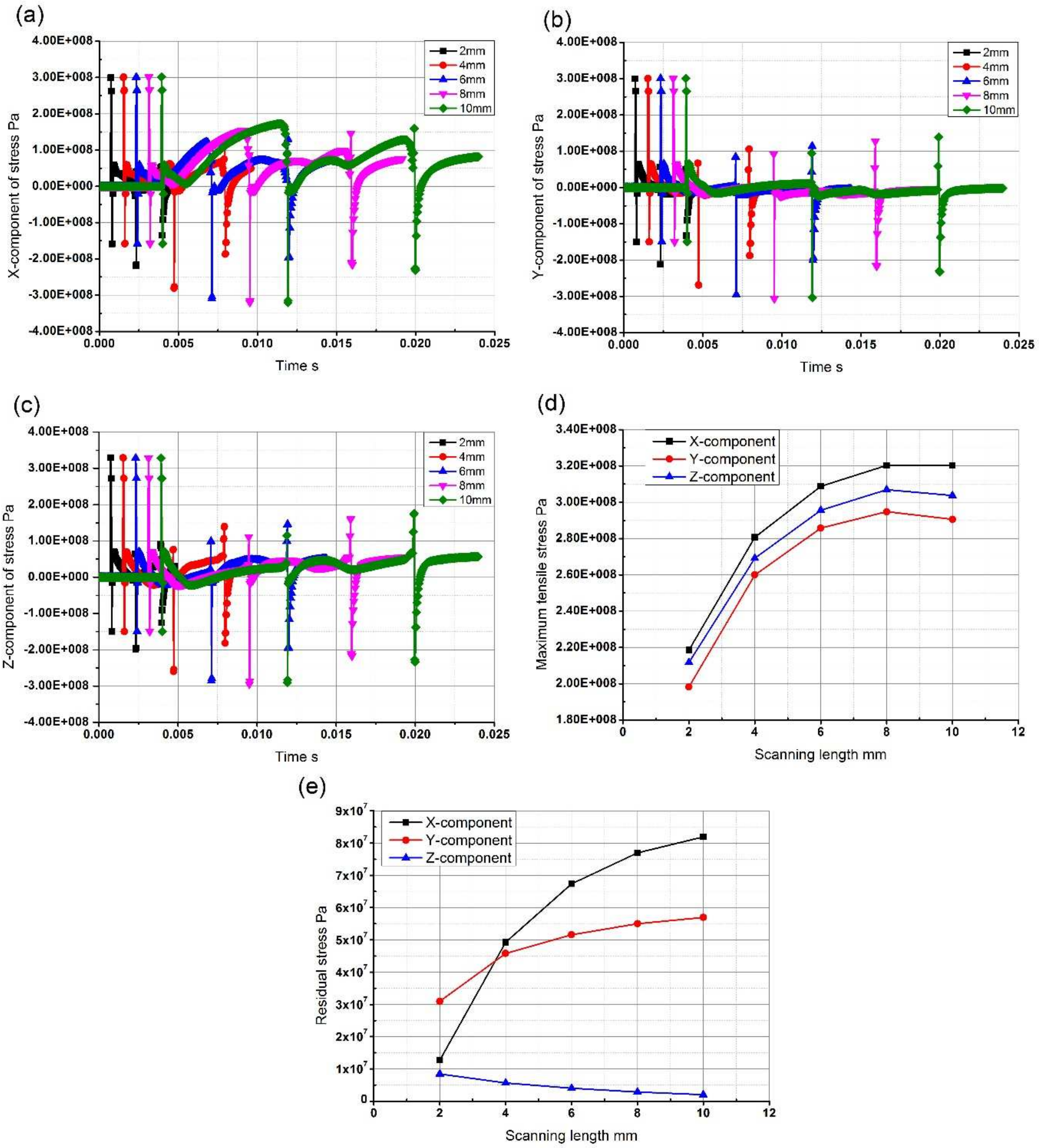

Fig. 14. Stress distributions of different scan lengths at Node 2 (a) X-component of stress; (b) Y-component of stress; (c) Z-component of stress; (d) Maximum tensile stress and (e) Residual stress

As more layers are fabricated, previously solidified layers prevent further deformation in the top layer. Since this mechanism occurs at each layer of the SLM process and accumulated deformation takes on the already solidified layers, a very high level of residual stresses can develop inside the built parts. On this account, the SLM components should be stress relieved through a heat-treated process before any other post-processing, such as the removal of the parts from the substrate. Otherwise, undesirable plastic deformation may occur because of stress relaxation [4].

The shrinkage of the thin-walled parts fabricated by SLM technology is affected by many exposure parameters, e.g. beam compensation, contouring and hatching, part orientation, compensation positioning, scan length and laser power, etc. [34]. The diameter of the molten pool is always bigger than that of the laser beam and is usually called as spot diameter. The laser beam must be offset at the contour of the object so as to compensate for the size deviation because of the spot diameter. In order to eliminate the effect of beam compensation, the test specimen (scan length=2mm) is selected as a reference due to its deviation, which is less affected by stress, and then the specimen's deviation along the scan direction is mainly decided by stresses and strains. As the balance of linear form in the X direction of the thin-walled part is more unstable for longer scan length specimens, residual stress has a growing impact on the deformation along the scan vector when the scan length increases. The thin-walled parts manufactured in SLM are illustrated in Fig. 15.

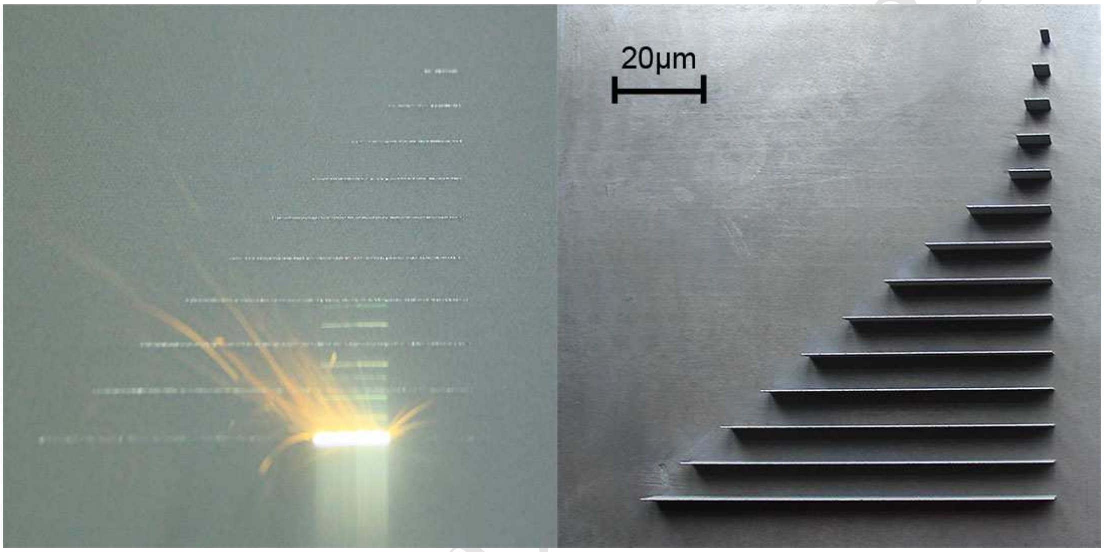

Fig. 15. Thin-wall parts built in SLM

Fig. 16 describes the deviations along the scan vector of the simulation and the experiment. The specimen's deviation is calculated by Eq. (16). The thin-walled parts' lengths are measured three times and the average value is acquired to represent the length of the parts for reducing the measurement error as far as possible. Deviations of the simulation are in strong agreement with the experimental results when the scan length is less than 50mm, but the simulation results do not fit well with the experiment data in long scan lengths as shown in Fig. 16(a). A calibrated simulation mode is introduced by considering the effect of the residual stress along the scan direction. The modified simulation results are consistent with the experiment data both in the short and long scan length. Deviations of the simulation are approximately proportional to the scan length. The linear fits of the simulation and the experiment are indicated in Fig. 16(b). The calibrated simulation results are closer to the experiment data. According to the results of the linear fits, the gaps between the simulation and the experiment increase with the scan length when the length exceeds 20 mm. As previously discussed, the residual stress has a great influence upon the deformation along the scan vector for the long length parts, which are easy to bend into an undesirable shape. Stress relaxation may lead to larger plastic deformation for the long thin-walled components.

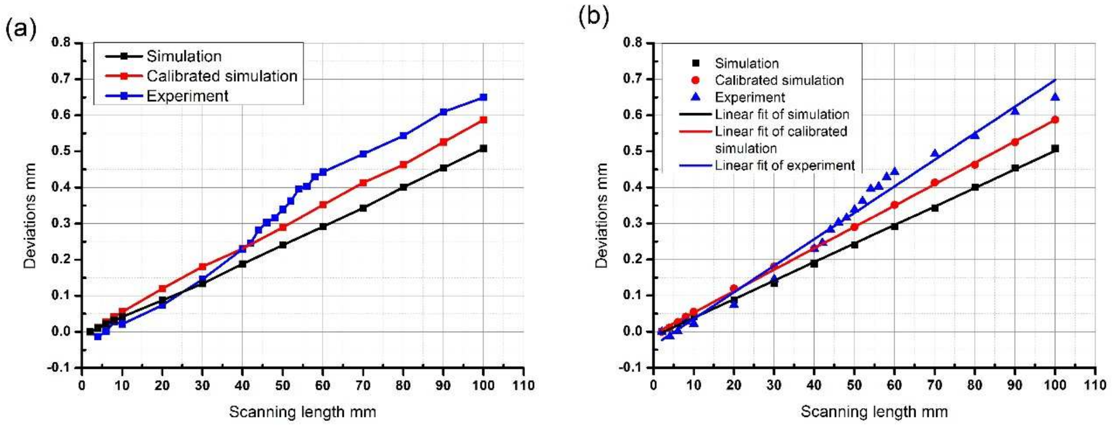

Fig. 16. Influence of scan length on shrinkage pattern (a) comparison of the shrinkage of simulation and experiment and (b) linear fit of the shrinkage

Fig. 17 shows the percentage shrinkage per unit length calculated by Eq. (17) in the scan length direction. The experiment's results fit the third-order polynomial based on the least squares theory. The shrinkage per length rises as the scan length grows. When satisfying the mechanical properties, the scan length is one of the most crucial factors. The most suitable scan length of the thin-walled part is between 4mm and 6mm as the shrinkage per unit in the scanning direction is taken into account. The shrinkage per unit is quite close to zero with the process parameters listed in Table 1 only when 4mm to 6mm were chosen as the scan lengths.

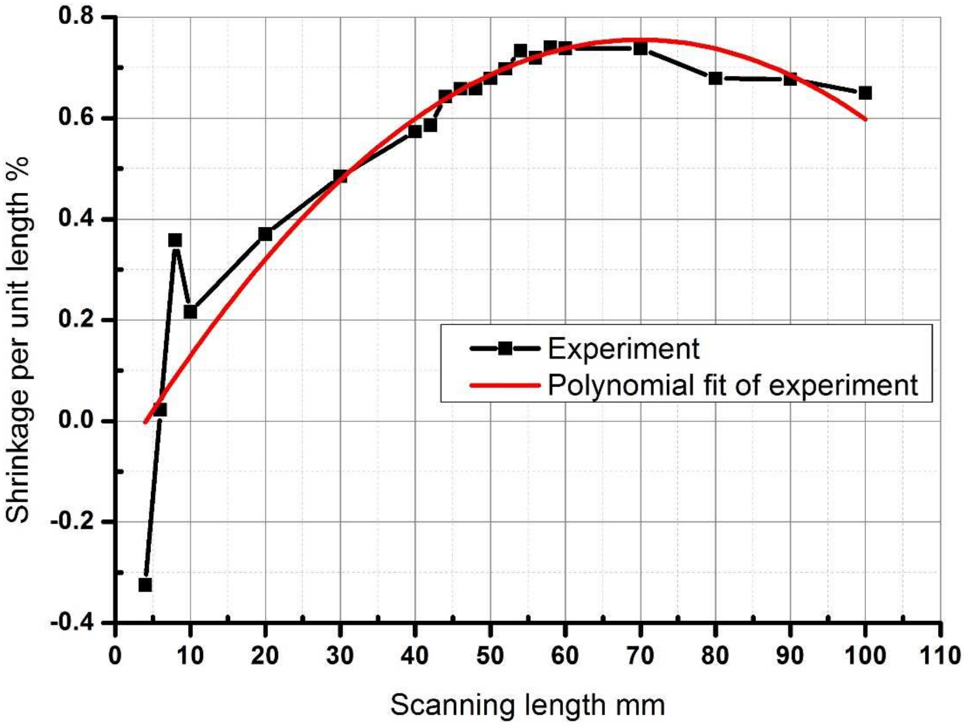

Fig. 17. The shrinkage per unit length of different scan lengths

5. Conclusion

The 3D transient indirect sequentially coupled thermal-structural finite element analysis model is applied to express the temperature, stress, and strain fields within a single scanning layer of the thin-walled components in the SLM process. The conclusions can be highlighted as follows.

- The difference among the peak temperatures of different scan lengths is small, whilst the second highest temperatures vary considerably.
- According to the molten pool dimension computed from the temperature field, the fully dense part can be fabricated with the hatch space of 0.1mm and the layer thickness of 0.03mm.
- The dramatic variations occur in the stress field during the process, and three directional stresses are cyclic tensile-compressive-tensile stresses.
- Deviations of the simulation are approximately proportional to the scan length. When residual stresses are taken into consideration, the deviations of the simulation are in strong agreement with the experimental results both in the short and the long scan length.
- According to the shrinkage per unit of built thin-walled parts with specified exposure strategies, the most appropriate scan length is between 4mm and 6mm.

In terms of the potential applications of the study, the results presented here can be used in industry for manufacturing high accuracy parts with thin-walled structures. One limitation of the study is that only one layer of thickness was studied; different layer thicknesses might generate different results. Therefore, the relevant study should be carried out for different layer thicknesses in future works.

Acknowledgement

The authors gratefully appreciate the financial support from the National High-tech Research and Development Program of China (2015AA042501). All authors thank to the valuable comments and suggestions of the editors and the anonymous referees which helped improve the presentation and quality of the manuscript.

References

1. Tolochko NK, Arshinov MK, Gusarov AV, Titov VI, Laoui T, Froyen L (2003) Mechanisms of selective laser sintering and heat transfer in Ti powder. Rapid Prototyping Journal 9 (5):314–326. doi:http://dx.doi.org/10.1108/13552540310502211
2. Zeng K, Pal D, Stucker B (2012) A review of thermal analysis methods in Laser Sintering and Selective Laser Melting. Paper presented at the 23rd Annual International Solid Freeform Fabrication Symposium Austin, Tx,
3. Guan K, Wang Z, Gao M, Li X, Zeng X (2013) Effects of processing parameters on tensile properties of selective laser melted 304 stainless steel. Materials & Design 50:581-586. doi:10.1016/j.matdes.2013.03.056
4. Hussein A, Hao L, Yan C, Everson R (2013) Finite element simulation of the temperature and stress fields in single layers built without-support in selective laser melting. Materials & Design 52:638-647. doi:10.1016/j.matdes.2013.05.070
5. Liu J, Li L: Effects of powder concentration distribution on fabrication of thin-wall parts in coaxial laser cladding. Optics & Laser Technology 2005, 37:287-292.
6. Chao Y-p, Qi L-h, Xiao Y, Luo J, Zhou J-m: Manufacturing of micro thin-walled metal parts by micro-droplet deposition. Journal of Materials Processing Technology 2012, 212:484-491.
7. Luo J, Pohl R, Qi L, Romer GW, Sun C, Lohse D, Visser CW: Printing Functional 3D Microdevices by Laser-Induced Forward Transfer. Small 2017, 13.

8. Clijsters S, Craeghs T, Moesen M, Kruth JP: Optimization of thin wall structures in SLM. Journal of Mathematical Sciences 2012, 104:847-880.
9. Abele E, Stoffregen HA, Kniepkamp M, Lang S, Hampe M (2015) Selective laser melting for manufacturing of thin-walled porous elements. Journal of Materials Processing Technology 215:114-122. doi:10.1016/j.jmatprotec.2014.07.017
10. Yadroitsev I, Shishkovsky I, Bertrand P, Smurov I (2009) Manufacturing of fine-structured 3D porous filter elements by selective laser melting. Applied Surface Science 255 (10):5523-5527. doi:10.1016/j.apsusc.2008.07.154
11. Kolossov S, Boillat E, Glardon R, Fischer P, Locher M (2004) 3D FE simulation for temperature evolution in the selective laser sintering process. International Journal of Machine Tools and Manufacture 44 (2-3):117-123. doi:10.1016/j.ijmachtools.2003.10.019
12. Song B, Dong S, Liao H, Coddet C (2011) Process parameter selection for selective laser melting of Ti6Al4V based on temperature distribution simulation and experimental sintering. The International Journal of Advanced Manufacturing Technology 61 (9-12):967-974. doi:10.1007/s00170-011-3776-6
13. Contuzzi N, Campanelli SL, Ludovico AD (2011) 3D Finite Element Analysis in the selective laser melting process. International Journal of Simulation Modelling 10 (3):113-121. doi:10.2507/ijsimm10(3)1.169
14. Roberts IA, Wang CJ, Esterlein R, Stanford M, Mynors DJ (2009) A three-dimensional finite element analysis of the temperature field during laser melting of metal powders in additive layer manufacturing. International Journal of Machine Tools and Manufacture 49 (12-13):916-923. doi:10.1016/j.ijmachtools.2009.07.004
15. Li Y, Gu D (2014) Parametric analysis of thermal behavior during selective laser melting additive manufacturing of aluminum alloy powder. Materials & Design 63:856-867. doi:10.1016/j.matdes.2014.07.006
16. H C, J J (1959) Conduction of heat in solids. 2nd ed 1
17. Chen W, Yang Y, Lee H (2007) Estimating the absorptivity in laser processing by inverse methodology. Applied Mathematics and Computation 190 (1):712-721. doi:10.1016/j.amc.2007.01.077
18. Frewin MR, Scott DA (1999) Finite element model of pulsed laser welding. Welding Research Supplement 15–22
19. Kruth JP, Wang X, Laoui T, Froyen L (2003) Lasers and materials in selective laser sintering. Assembly Automation 23 (4):357–371. doi:http://dx.doi.org/10.1108/01445150310698652
20. Ready JF (1971) Effects of High-Power Laser Radiation. Elsevier Science edn. Academic Press, New York
21. Fischer P, Romano V, Weber HP, Karapatis NP, Boillat E, Glardon R (2003) Sintering of commercially pure titanium powder with a Nd:YAG laser source. Acta Materialia 51 (6):1651-1662. doi:10.1016/s1359-6454(02)00567-0
22. Thummler F, Oberacker R (1993) An Introduction to Powder Metallurgy. Maney Publishing, London
23. Rombouts M, Froyen L, Gusarov AV, Bentefour EH, Glorieux C (2005) Light extinction in metallic powder beds: Correlation with powder structure. Journal of Applied Physics 98 (1):013533/013531-013533/013539. doi:10.1063/1.1948509
24. Gusarov AV, Yadroitsev I, Bertrand P, Smurov I (2007) Heat transfer modelling and stability analysis of selective laser melting. Applied Surface Science 254 (4):975-979. doi:10.1016/j.apsusc.2007.08.074
25. Mills KC (2002) Recommended Values of Thermophysical Properties for Selected Commercial alloys. Woodhead Publishing Ltd, Cambridge
26. Yilbas BS, Arif AFM (2001) Material response to thermal loading due to short pulse laser heating. Internation Journal of Heat and Mass Transfer 44 (20):3787-3798. doi:10.1016/S0017-9310(01)00026-6
27. xiangqian K (1999) Thermal stress analysis of finite element method. SHANGHAI JIAO TONG UNIVERSITY PRESS, Shanghai
28. Yu g, Yu h (2012) Laser manufacturing technology. Nation defense industy press, Beijing
29. Kawamura Y, Liu H-B, Inoue A, Masumoto T (1997) Rapidly solidified powder metallurgy Al-Ti-Fe alloys. Scripta Materialia 37 (2):6. doi:10.1016/S1359-6462(97)00080-8

30. Dai K, Shaw L (2002) Distortion minimization of laser-processed components through control of laser scanning patterns. Rapid Prototyping Journal 8 (5):270-276. doi:http://dx.doi.org/10.1108/13552540210451732
31. Su X, Yang Y (2012) Research on track overlapping during Selective Laser Melting of powders. Journal of Materials Processing Technology 212 (10):2074-2079. doi:10.1016/j.jmatprotec.2012.05.012
32. Gu D, Shen Y (2009) Balling phenomena in direct laser sintering of stainless steel powder: Metallurgical mechanisms and control methods. Materials & Design 30 (8):2903-2910. doi:10.1016/j.matdes.2009.01.013
33. Matsumoto M, Shiomi M, Osakada K, Abe F (2002) Finite element analysis of single layer forming on metallic powder bed in rapid prototyping by selective laser processing. International Journal of Machine Tools & Manufacture 42 (1):61-67. doi:10.1016/S0890-6955(01)00093-1
34. Senthilkumaran K, Pandey PM, Rao PVM (2009) Influence of building strategies on the accuracy of parts in selective laser sintering. Materials & Design 30 (8):2946-2954. doi:10.1016/j.matdes.2009.01.009

Highlights:

1. The paper studied the relationship between the scan lengths and distributions of temperature and stress fields of thin-walled parts in the SLM process, using FEA and the experiment method.
2. It is found that the scan length chiefly affects the second peak temperature rather than the highest temperature.
3. The deviations of the thin-walled parts are approximately proportional to the scan lengths.
4. The most suitable scan length is between 4mm and 6mm for the thin-walled components with specified process parameters.